The Astronomical Journal, 159:138 (17pp), 2020 April https://doi.org/10.3847/1538-3881/ab6efb

Stellar Mass and Stellar Mass-to-light Ratio–Color Relations for Low Surface Brightness Galaxies

Wei Du[1,2], Cheng Cheng[3], Zheng Zheng[1,4], and Hong Wu[1,2]
[1] National Astronomical Observatories, Chinese Academy of Sciences (NAOC), 20A Datun Road, Chaoyang District, Beijing 100012, People's Republic of China
wdu@nao.cas.cn
[2] Key Laboratory of Optical Astronomy, NAOC, 20A Datun Road, Chaoyang District, Beijing 100012, People's Republic of China
[3] Chinese Academy of Sciences South America Center for Astronomy, National Astronomical Observatories, CAS, Beijing 100101, People's Republic of China
[4] Chinese Academy of Sciences Key Laboratory of FAST, NAOC, 20A Datun Road, Chaoyang District, Beijing 100012, People's Republic of China; zz@nao.cas.cn
Received 2019 August 16; revised 2020 January 2; accepted 2020 January 21; published 2020 March 3

Abstract

We estimate the stellar mass for a sample of low surface brightness galaxies (LSBGs) by fitting their multiband spectral energy distributions (SEDs) to the stellar population synthesis model. The derived stellar masses (log $M_*/M_\odot$) span from 7.1 to 11.1, with a mean of log $M_*/M_\odot = 8.5$, which is lower than that for normal galaxies. The stellar mass-to-light ratio (γ^*) in each band varies little with the absolute magnitude but increases with higher M_*. This trend of γ^* with M_* is even stronger in bluer bands. In addition, the γ^* for our LSBGs slightly declines from the r band to the longer-wavelength bands. The log γ^j_* ($j = g$, r, i, and z) have relatively tight relations with optical colors of $g - r$ and $g - i$. Compared with several representative γ^*–color relations (MLCRs) from the literature, our MLCRs based on LSBG data are consistently among those literature MLCRs previously defined on diverse galaxy samples, and the existing minor differences between the MLCRs are caused by the differences in the SED model ingredients (including initial mass function, star formation history, and stellar population model), line fitting techniques, galaxy samples, and photometric zero-point, rather than the galaxy surface brightness itself, which distinguishes LSBGs from high surface brightness galaxies. Our LSBGs would be very likely to follow those representative MLCRs previously defined in diverse galaxy populations, if those main ingredients were taken into account.

Unified Astronomy Thesaurus concepts: Low surface brightness galaxies (940); Mass-to-light ratio (1011); Surface photometry (1670); Galaxy masses (607)

1. Introduction

Galaxies with central surface brightnesses fainter than the night sky (∼22.5 B mag arcsec^{-2}) are defined as low surface brightness galaxies (LSBGs; e.g., Impey & Bothun 1997; Impey et al. 2001; Ceccarelli et al. 2012). In the local universe, LSBGs take up a fraction of ∼30%–60% in number (e.g., McGaugh et al. 1995; McGaugh 1996; Bothun et al. 1997; O'Neil et al. 2000; Trachternach et al. 2006; Haberzettl et al. 2007) and ∼20% in dynamical mass (e.g., Minchin et al. 2004) among all galaxies. Generally speaking, LSBGs are abundant in H I gas but deficient in metal ($\leqslant 1/3$ solar abundance) and dust (e.g., McGaugh & Bothun 1994; Matthews et al. 2001), and they have fairly low star formation rates (SFRs; e.g., Das et al. 2009; Galaz et al. 2011; Lei et al. 2018), which is evidence that only a small number of H II regions inhabit their diffuse disks. They also have lower stellar mass densities compared to their high surface brightness galaxy (HSBG) counterparts (normal galaxies; e.g., de Blok et al. 1996; Burkholder et al. 2001; O'Neil et al. 2004; Trachternach et al. 2006). These special properties imply that LSBGs could have different formation and evolutionary histories from normal galaxies (e.g., Huang et al. 2012).

Galaxy stellar mass, M_*, is a critical physical property for studying galaxy formation and evolution because its growth is directly related to galaxy formation and evolution. A widely used simple method to estimate M_* is to multiply the measured galaxy luminosity, L, with a fixed stellar mass-to-light ratio (γ^*). However, different stellar populations have very different spectral energy distributions (SEDs), with younger stars dominating bluer bands and older stars dominating redder bands. Therefore, the γ^*s in different bands need to be calibrated separately for different populations and photometric bands. In this case, the technique of modeling the broadband photometry (SED fitting) to stellar population synthesis (SPS) models is used to estimate the stellar mass of the galaxy. Usually, the stellar masses for "normal" galaxies (i.e., not including pathological star formation histories (SFHs)) can be recovered at the ∼0.3 dex level (1σ uncertainty) by the broadband SED fitting. This uncertainty does not include potential systematics in the underlying SPS models (Conroy 2013). Then, another convenient technique to derive the galaxy stellar mass is to use the relation between color and γ^* of the galaxies. So far, the γ^*s in different photometric broad bands have been derived as a function of galaxy colors by various studies (e.g., Bell & de Jong 2001; Bell et al. 2003; Portinari et al. 2004; Zibetti et al. 2009; McGaugh & Schombert 2014). However, the existing prescriptions are mostly calibrated for normal galaxies, which have very different properties from LSBGs. The star-forming main sequence (log SFR–log M_*) of dwarf LSBGs has a steep slope of approximately unity, distinct from the shallower slope of more massive spirals (McGaugh et al. 2017). Generally, a slope of unity would agree with galaxies forming early in the universe and subsequently forming stars at a nearly constant specific SFR (sSFR). In contrast, a shallow slope implies that low-mass galaxies were

formed recently in a shorter timescale with a higher sSFR (sSFR is roughly inversely proportional to the age of the stellar disk). These different formation scenarios could potentially lead to different γ^*s. Therefore, we estimate the γ^*s and stellar masses of a sample of over 1000 LSBGs defined in the previous work of Du et al. (2015, 2019) by fitting their multiband (from UV to near-IR (NIR)) SEDs to the stellar population models and investigate the correlations between the γ^* and observed colors for the LSBG sample.

We briefly introduce the LSBG sample and show the multiwavelength photometric band data in Section 2. We then show data reduction and photometry in Section 3. We demonstrate the multiband SED fitting process and show the derived LSBG stellar mass distribution in Section 4. We explore the distributions of the derived LSBG M/Ls and their correlations with galaxy colors in Section 5 and discuss the results in Section 6. Throughout this paper, the distances we used to convert apparent magnitude to absolute magnitude and luminosity are from the ALFALFA catalog (Haynes et al. 2018), which adopted the Hubble constant of $H_0 = 70\,\mathrm{km\ s^{-1}\ Mpc^{-1}}$. Magnitudes in this paper are all in the AB magnitude system.

2. Sample and Data

2.1. LSBG Sample

We have selected a sample of 1129 LSBGs from the combination of the α.40 H I survey (Haynes et al. 2011) and the Sloan Digital Sky Survey (SDSS) DR7 photometric survey (Abazajian et al. 2009). We briefly introduce the sample selection and properties below, and details and related studies can be found in Du et al. (2015, 2019).

The LSBGs are very sensitive to the sky background, so it is crucial to precisely subtract the sky background from the galaxy image before photometry. Unfortunately, the sky backgrounds have been overestimated by the SDSS photometric pipeline for galaxy images in their *ugriz* bands, which consequently results in an average underestimation of ∼0.2 mag in luminosity of bright galaxies (Lauer et al. 2007; Liu et al. 2008; Hyde & Bernardi 2009; He et al. 2013) and ∼0.5 mag of LSBGs (Lisker et al. 2007). To improve the sky subtraction, we reestimate the sky background of *g*- and *r*-band images for each galaxy in the α.40–SDSS DR7 sample using a fully tested method of sky estimation (Zheng et al. 1999). The method fits all of the sky pixels on the object-masked image row-by-row and column-by-column and is designed for a better estimate of the sky background map for galaxies with faint outskirts (Zheng et al. 1999; Wu et al. 2002) and LSBGs (Du et al. 2015). More details about this sky background estimation method and its applications for bright galaxies and LSBGs have been reported in Zheng et al. (1999), Wu et al. (2002), and Du et al. (2015). On sky-subtracted images in the *g* and *r* bands, we measure the magnitudes of galaxies using the SExtractor code (Bertin & Arnouts 1996) and fit the radial surface brightness profiles of galaxies to exponential profile models using the Galfit code (Peng et al. 2002). Then, the magnitude from SExtractor and the results from Galfit, including disk scale length, r_s, and minor-to-major axial ratio, b/a, are used to calculate the disk central surface brightness in the *g* and *r* bands, which are then combined to be converted to the disk central surface brightness in the *B* band, $\mu_0(B)$, according to the transformation formula of Smith et al. (2002). Finally, based on the traditional definition for LSBGs, we select 1129 non-edge-on galaxies ($b/a > 0.3$ in both the *g* and *r* bands) with $\mu_0(B) \geqslant 22.5$ mag arcsec^{-2} from the entire α.40–SDSS DR7 sample (12,423 galaxies) to form our LSBG sample.

Table 1
The Number of LSBG Scientific Images Available in Multi-passbands

Passband	Number
GALEX FUV	924
GALEX NUV	932
SDSS *u*	1129
SDSS *g*	1129
SDSS *r*	1129
SDSS *i*	1129
SDSS *z*	1129
UKIDSS *Y*	717
UKIDSS *J*	697
UKIDSS *H*	709
UKIDSS *K*	717

The H I–selected LSBG sample, inhabiting a low-density environment (Du et al. 2015) and dominated by dwarf galaxies in luminosity and late-type galaxies in morphology, has extended the parameter space covered by the existing LSBG samples to fainter luminosity, lower H I gas mass, and bluer color (Du et al. 2019). More details are available in Du et al. (2015, 2019).

2.2. Photometric Data

We collected the available scientific images for each galaxy of our LSBG sample in the far-UV (FUV) and NUV (*GALEX*; Martin et al. 2005), *ugriz* (SDSS DR7; York et al. 2000), and *YJHK* (UKIDSS LAS DR10; Lawrence et al. 2007) passbands. We note that the sky areas covered by different surveys do not completely overlap each other due to different survey strategies. Therefore, not all of the galaxies in our LSBG sample are available in all 11 passbands. We list the number of galaxies that are available in each of the 11 passbands in Table 1. All of the LSBGs in our sample have been observed by the SDSS DR7. However, combining the optical with the UV bands, 924 galaxies are available in both the SDSS DR7 and *Galaxy Evolution Explorer* (*GALEX*) DR6 surveys. Combining the optical with the NIR bands, 672 galaxies have been observed by both the SDSS DR7 and UKIDSS LAS DR10 surveys. Furthermore, combining the optical, UV, and NIR, only 544 galaxies are available in all 11 bands.

2.3. Multiband Photometry

2.3.1. Image Reduction

The scientific images for galaxies in our LSBG sample are all bias-subtracted, dark-subtracted (only for NIR frames), flat-fielded, and flux-calibrated by the survey teams. We just need to start the data reduction from sky subtraction.

As for the UV sky background, we directly use the sky background map provided by the *GALEX* team. However, for the optical and NIR bands, only an average sky value is provided for a galaxy image by SDSS DR7 or UKIDSS LAS DR10, not to mention the problem of overestimation of sky background by the SDSS DR7 photometric pipeline (see Section 2). So, we estimate the sky background map for the

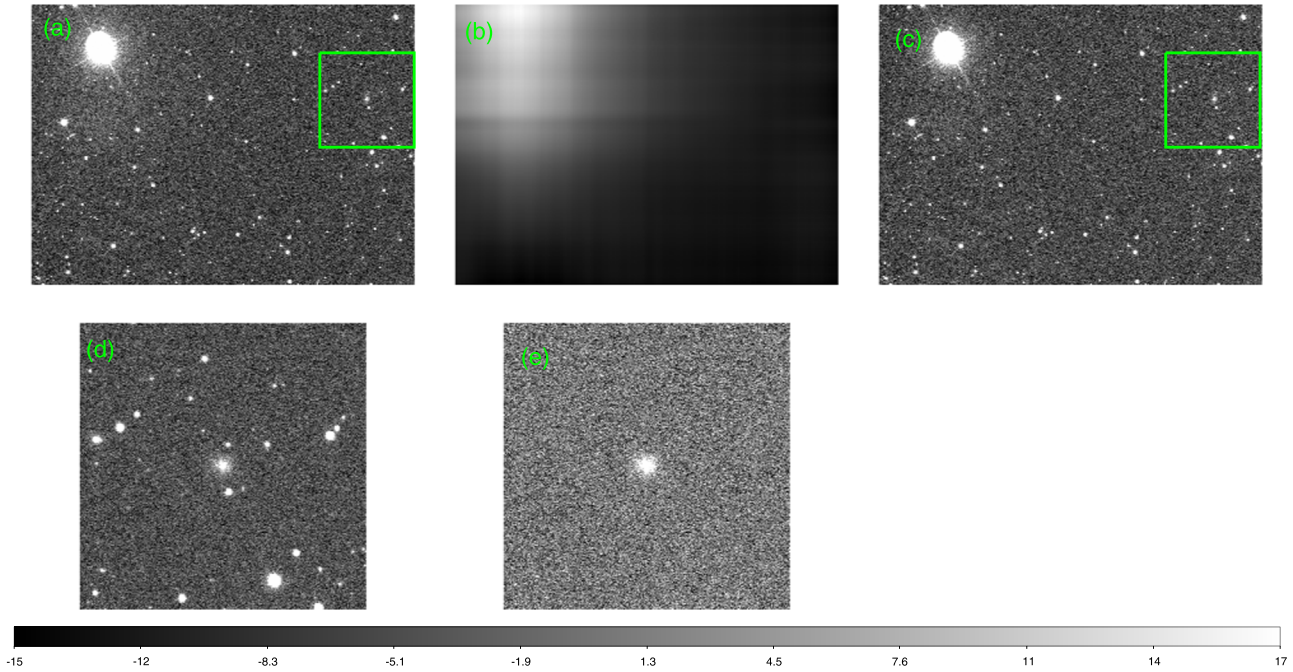

Figure 1. Reduction of the SDSS *r*-band image of the example LSBG AGC 192669. Panel (a) shows the original *r*-band scientific image frame from SDSS DR7, with AGC 192669 centered in the green square of size $200'' \times 200''$. Panel (b) displays the sky background map we constructed by using the row-by-row and column-by-column fitting method (Zheng et al. 1999). Panel (c) shows the sky-subtracted image, which is produced by subtracting the sky background map (panel (b)) from the original galaxy image (panel (a)). Panel (d) shows the region within the green square of the size $200'' \times 200''$, centered on the center of the galaxy AGC 192669. On the trimmed image, we masked all other objects (except for the central target galaxy itself) detected by SExtractor and generated the image in panel (e) by replacing the pixel values within the masked regions with the average background value. The image shown in panel (e) is for further photometric measurements.

LSBG image in each of the *ugriz* and *YJHK* bands using the row-by-row and column-by-column fitting method (Zheng et al. 1999) on the image, with all detected objects being masked out. As a fully tested sky estimation method, it has been successfully practiced for bright galaxies with faint extended outskirts (Zheng et al. 1999; Wu et al. 2002) and for LSBGs (Du et al. 2015), and the details are specified in Section 3.1 of Du et al. (2015).

After subtracting the sky background for the LSBG image, we use SExtractor (Bertin & Arnouts 1996) to make a systematic, homogeneous photometric measurement on the LSBG images of all 11 bands by performing the pixel-to-pixel photometry in dual-image mode. In dual-image mode, the galaxy image in the *r* band is used as a reference for source detection and photometric aperture definition (center position, size, and shape); then, images in all other passbands for the galaxy are photometrically measured within the same aperture as defined by the reference image. So, the dual-image mode of SExtractor requires that galaxy images in all passbands must match with the reference image in dimension, orientation, pixel scale, image size, and object position. We use the *r*-band galaxy image with sky subtracted as the reference, so we have to resample the sky-subtracted images of the galaxy in all other bands (FUV, NUV, *ugiz*, and *YJHK*) using cubic interpolations to match with the reference image in image orientation, pixel scale, image size, and object position. The matched images in all bands are then trimmed to have an equal size of $200'' \times 200''$, with the target galaxy at the center of the trimmed image. Then, we keep the centering galaxy (target) on each trimmed image and mask all other detected objects (by SExtractor with 3σ as the minimum detection threshold) from the trimmed image to avoid the light contamination from adjacent objects. We then fill the masked regions with average values of the background pixel of each object-masked image. Such reduced images are ready for further photometry in Section 2.3.2. For a better illustration of the image reduction process, we take the *r*-band image of the galaxy AGC 192669 in our LSBG sample as an example in Figure 1, where panels (a) and (c), respectively, show the original and sky-subtracted image frames. In order to more clearly demonstrate the quality of our sky subtraction, we compare the distribution of the background pixel values of the sky-subtracted image (panel (c)) with the distribution of the background pixel values of the original image (panel (a)) with a simple mean background value subtracted from in Figure 2, where the image background is closer to zero after our sky subtraction (black line).

2.3.2. Photometry

We used SExtractor to define the position and aperture of the galaxy in the *r*-band image and then used the *r*-band position and aperture information to measure the galaxy magnitude within each filter of FUV, NUV, *u*, *g*, *r*, *i*, *z*, *Y*, *J*, *H*, and *K* (using the SExtractor dual-image mode). As the aperture definitions do not vary between wave bands, this measurement gives internally consistent colors. The measured magnitudes in all bands are corrected for Galactic extinction using the prescription of Schlafly & Finkbeiner (2011). We show the aperture of the galaxy AGC 192669 in a reduced image in each band in Figure 3, for example.

This aperture is the automatic aperture (AUTO), as among the various magnitude types that SExtractor provides (isophotal, corrected isophotal, fixed aperture, AUTO, and Petrosian), the AUTO, inspired by Kron's "first moment" algorithm (see details in Kron 1980), is a flexible and accurate elliptical aperture whose elongation ϵ and position angle θ are defined by the second-order moments of the object's light

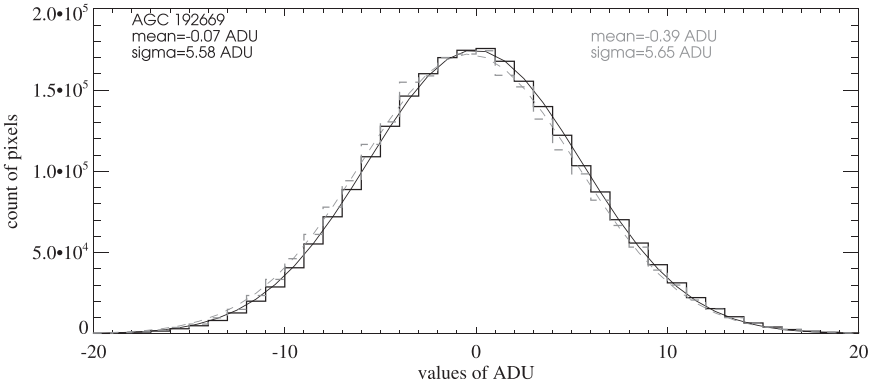

Figure 2. Distributions of the pixel values of all of the unmasked region (with the object masked during our sky estimation process) of the sky-subtracted image frame of AGC 192669. The solid black line represents the sky-subtracted frame by our sky subtraction method of piecewise row-by-row and column-by-column fitting, and, for comparison, the dashed gray line is for the frame without our accurate sky background subtraction but only with the simple mean value of all of the unmasked region subtracted (similar to the SDSS method, which gives a single sky value for an image frame). It demonstrates that the mean background value is closer to zero after applying our sky subtraction method.

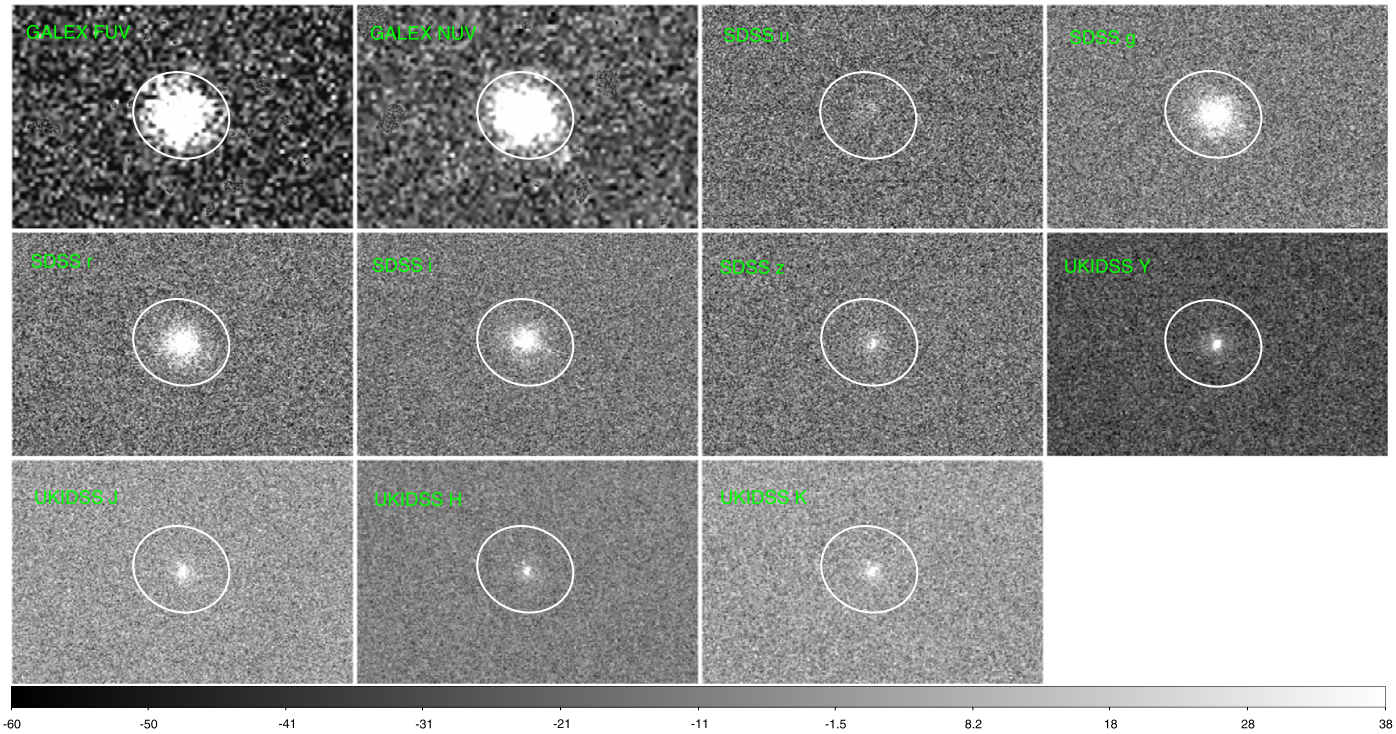

Figure 3. Homogeneous photometric apertures of the example LSBG AGC 192669 in multiple bands from *GALEX* FUV and NUV; SDSS u, g, r, i, z; and UKIDSS Y, J, H, and K.

distribution. Within this aperture, the characteristic radius r_1 is defined as $r_1 = \frac{\sum rI(r)}{\sum I(r)}$, which is weighted by the light distribution function. Kron (1980) and Infante (1987) verified that, for stars and galaxy profiles convolved with a Gaussian, more than 90% of the flux is expected to lie within a circular aperture of radius kr_1 if $k = 2$, almost independent of their magnitudes. This changes if an ellipse with ϵ kr_1 and $\frac{kr_1}{\epsilon}$ are considered as the principal axes. By choosing a larger $k = 2.5$, more than 96% of the flux is captured within the elliptical aperture. So, the AUTO magnitudes are intended to give the more precise estimate of "total magnitudes," at least for galaxies. More details about the AUTO photometry can be found in the SExtractor manual and Kron (1980), Infante (1987), and Bertin & Arnouts (1996). During our measurements, we keep $k = 2.5$, the setting recommended by SExtractor (Bertin & Arnouts 1996), and the following studies will be based on the AUTO magnitude in the AB magnitude system.

3. Stellar Mass

Galaxies emit electromagnetic radiation over the full possible wavelength range, and the distribution of energy over wavelength is called the SED, which is our primary source of information about the properties of the unresolved galaxy. In general, the different physical processes occurring in galaxies all leave their imprints on the global and detailed shapes of the spectra or SEDs. Therefore, we can constrain the galaxy stellar mass by fitting models to its SED. In Section 2.3.2, we derived the multiband magnitudes of each LSBG in our sample, so we can construct the SED for each LSBG. Since the UV light

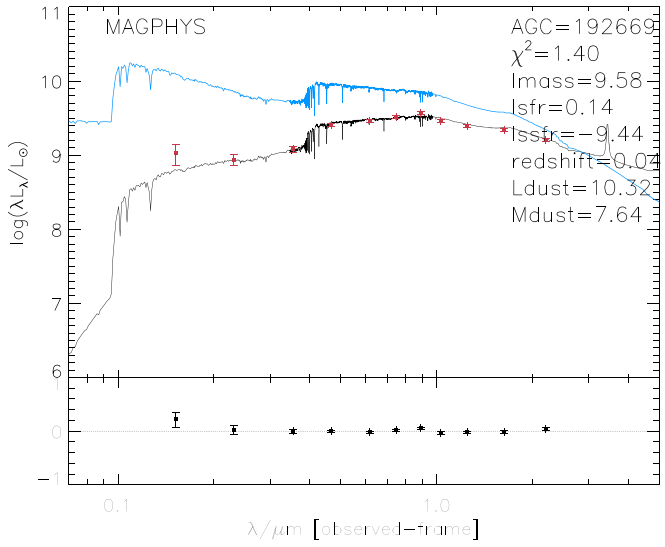

Figure 4. Best fit for the SED of the LSBG AGC 192669 by using MAGPHYS (top). The best-fitting model (black curves) to the observed SED (red filled squares) is shown in the top panel, and the residual between the model and observation is shown in the bottom panels. The blue curve in the MAGPHYS panel shows the unattenuated model spectrum. Additionally, the stellar mass (lmass), SFR (lsfr), log sSFR (lssfr), redshift, and dust (Ldust and Mdust) given by the best-fitting model are listed in the panel.

comes from regions where hot and young stars reside, and the NIR light is the best tracer of old stars that dominate the stellar mass of a galaxy, our SEDs covering multiple bands from UV to NIR allow us to include the contribution of both young and old stars to stellar mass. It should be noted that for the LSBGs, which have not been observed in all 11 bands, we only use the available bands to construct the SED.

3.1. SED Fitting

MAGPHYS (da Cunha et al. 2008) is one of the widely used SED fitting codes (e.g., Zheng et al. 2015) that uses the 2007 version of the Bruzual & Charlot (2003) SPS model (CB07) covering a wavelength range from 91 Å to 160 μm, different ages from 0.1 Myr to 20 Gyr, and various metallicities (Z) from 0.02 to 2 times solar. The SFH is described by an underlying continuous model (exponentially declining star formation) with instantaneous bursts superimposed. The initial mass function (IMF) of Chabrier (Chabrier 2003) is assumed, and the simple two-component dust model of Charlot & Fall (2000) is adopted to describe the attenuation of the stellar light by the dust. Using MAGPHYS (da Cunha et al. 2008), we fit the SPS models to the multiband SED of each LSBG in our sample to estimate the galaxy stellar mass. For example, we show the best-fitting model and residual by using MAGPHYS for the LSBG (AGC 192669 in the top two panels of Figure 4). We note that MAGPHYS gives both the stellar mass of the best-fitting model and the stellar mass distribution. In this paper, we use the mean value of the stellar mass from the given stellar mass distribution as our derived galaxy stellar mass, M_*.

Checking the fitting results from MAGPHYS, we found that MAGPHYS always gives the lower limit of the model in stellar mass for 77 galaxies out of the total LSBG sample (1129 galaxies), so we would exclude these 77 galaxies in subsequent analysis, and the sample for further investigation includes 1052 LSBGs (research sample (R sample)). In order to check whether the R sample (1040 LSBGs) is representative of the total LSBG sample (T sample; 1129 LSBGs), we compare them in terms of physical properties in Figure 5. Compared with the T sample (black), the R sample (green) has quite similar distributions in the main properties of magnitude, color, central surface brightness, size, and color versus H I mass, but it lacks the very low redshift, faint, and H I–poor galaxies. Therefore, the R sample is a good representative of our total LSBG sample, and our further analysis in this paper will be based on the R sample, which may still be named the LSBG sample later.

3.2. Stellar Mass Distribution

The derived stellar masses using MAGPHYS are shown in Figure 6 for the R sample, ranging from log $M_*/M_\odot \sim 7.1$ to 11.1, with a mean log $M_*/M_\odot = 8.47$ and a median log $M_*/M_\odot = 8.48$ for the R LSBG sample, which is considerably lower than the stellar mass for the normal galaxies. Furthermore, LSBGs that have lower surface brightnesses (fainter than 25.0 mag arcsec^{-2}) tend to have lower stellar mass, and LSBGs that have higher stellar masses tend to have higher surface brightnesses (right panel of Figure 6).

4. Stellar γ^*

The best approach to measure γ^* is to fit SEDs simultaneously in multiple passbands, with at least one in the NIR to break the age–metallicity degeneracy. We show the γ^* derived from fitting the UV–optical–NIR SEDs of our galaxies in Figure 7. The UV is strongly affected by the young, luminous, blue stars formed in the recent SFH of a galaxy. These stars produce a large amount of the UV light and contribute most to the fluxes of galaxies, so having the UV band involved in the galaxy SED fitting should provide stronger constraints on the SFH, average age, metallicity, stellar mass, and γ^* of galaxies via the luminosity-weighted SED fitting. Compared to the average γ^* measured in the optical and NIR bands, the γ^* in the UV bands suffers more perturbations because those young, luminous, blue stars contribute little to the stellar mass of a galaxy (McGaugh & Schombert 2014), so it is not informative to investigate the γ^* in the UV bands derived from SED fitting. Here we only show the log γ^* measured in the optical *ugriz* and NIR *YJHK* bands for the R LSBG sample in Figures 7(a)–(i), and the log γ^* (γ^*) values are −0.48 (0.33), −0.40 (0.40), −0.33 (0.47), −0.40 (0.40), −0.39 (0.41), −0.40 (0.40), −0.46 (0.35), −0.55 (0.28), and −0.66 (0.22) in the *ugrizYJHK* bands, respectively, which are lower than the γ^* for normal galaxies. In Figure 7(j), the mean γ^* slightly declines as the wavelength band moves from r to K. Such a declining trend for the γ^* of the normal disk galaxies from V to [3.6] through I and K has been reported to be stronger (McGaugh & Schombert 2014). According to Figure 1 in Wilkins et al. (2013), the γ^*s measured at different wavelengths of a stellar population are dependent on the specific SED shape of the population, with a lower γ^* at the wavelength with a higher specific SED flux. So, the slight declining trend of γ^* of our sample from r to K implies that the overall LSBGs of our sample have a slightly rising SED shape from r to NIR.

In Figure 8, the γ^* measured in each band of *ugrizYJHK* is shown against the absolute magnitude (left column) and stellar mass (right column) for the R LSBG sample. While the distribution of γ^* in the z band for a sample of galaxies drawn from the SDSS main galaxy sample (bright galaxies with

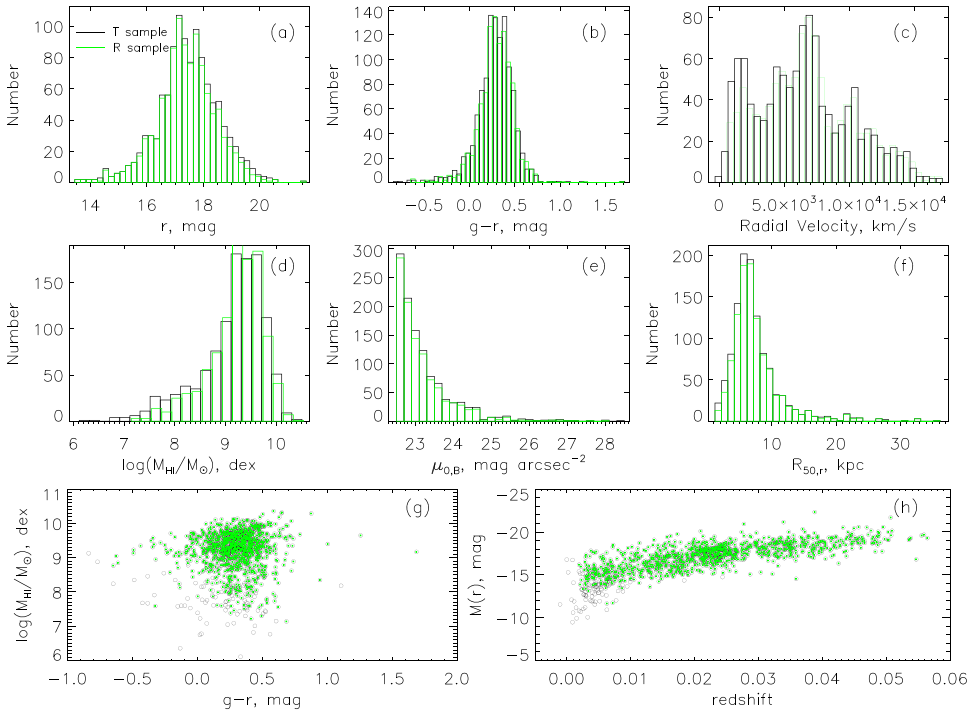

Figure 5. Properties of the R sample (green) in comparison with the T sample (black) in terms of (a) r-band magnitude, r; (b) optical color, g–r; (c) radial velocity, in km s^{-1}; (d) H I mass, $\log(M_{\rm H\,I}/M_\odot)$, in dex; (e) central surface brightness in the B band, $\mu_{0,B}$, in mag arcsec^{-2}; (f) effective radius, $R_{50,r}$, in kpc; (g) H I mass vs. g–r; and (h) r-band absolute magnitude vs. redshift.

Petrosian r-band magnitudes in the range of 14.5 mag $< r <$ 17.7 mag) is strongly dependent on galaxy luminosity (see Figure 13 of Kauffmann et al. 2003), it shows that the γ^* for the bright galaxies (e.g., brighter than around -13 mag in the r band) of our LSBG sample slowly changes with the absolute magnitude in any band from u to K (left column), as the slopes of the fitting lines are all around zero (within ±0.04) if we forced only the bright galaxies (with absolute magnitudes in the corresponding band brighter than -16 mag) to be fitted by a linear line in each panel of the left column. However, the γ^* for the R LSBG sample slightly increases with the galaxy stellar mass (right column), and this increasing trend (represented by the black dotted line, which is a linear fitting for all R LSBG sample galaxies) is stronger in shorter/bluer wavelength bands than longer/redder bands. This is quantitatively evidenced by the steepest slope of the fitting line in the u band (top panel) and the nearly flat slope of the fitting line in the K band (bottom panel) in Figure 8. Furthermore, the scatter of data points in γ^* in any band is becoming narrower at higher stellar mass (right column), indicating less diversity in SFH.

5. Color versus γ^*

5.1. Color–γ^* Relation for Our LSBGs

Various prescriptions for predicting γ^* from the observed colors have been previously calibrated for normal galaxies (e.g., Bell & de Jong 2001; Bell et al. 2003; Portinari et al. 2004; Zibetti et al. 2009; McGaugh & Schombert 2014). In contrast, our correlation is based on a sample of LSBGs that is dominated by dwarf LSBGs (Figure 1 in Du et al. 2019) with ~50% of the R sample fainter than $r = 17.5$ mag (Figure 2(b) in Du et al. 2019); almost all fainter than 21 mag arcsec^{-2} in r surface brightnesses, μ_r (Figure 2(d) in Du et al. 2019); and 73% bluer than $g - r = 0.4$ mag (Figure 5(b)). As the dwarf LSBGs have been reported to form a distinct sequence from more massive normal galaxies in the star-forming main sequence (McGaugh et al. 2017), we expect to study the MLCR based on our LSBG sample, which has a large fraction of dwarf LSBGs.

We fit the relations of γ^* measured in each of the *grizJHK* bands to the optical ($u-g$, $u-r$, $u-i$, $u-z$, $g-r$, $g-i$, $g-z$, $r-i$, and $r-z$) and NIR ($J-H$, $J-K$, and $H-K$) colors, respectively, for the LSBG sample in the form of $\log(\gamma^*) = a_\lambda + b_\lambda \times$ color. The fitting method is the bi-square-weighted line fitting method, which is the same as the fitting method that was used by the Bell et al. (2003) MLCRs. To test the goodness of the fit to our data, we calculate and show the Pearson correlation coefficient (PCC) for each of these fits in Table 2. The PCC is a measure of the linear correlation between two variables, and it has a value between +1 and −1, where +1 (−1) is a total positive (negative) linear correlation, and zero is no linear correlation. As shown in Table 2, using u colors as a γ^* estimator for our sample results in low PCCs (<0.5). This is presumably for two reasons. One reason is that, compared with relatively redder bands (g and r), the u band is more affected by the recently formed young stars, which would cause considerably more perturbations to the average γ^* in the u band than the g and r bands. Another reason might be the quality of the SDSS u-band images, which are reported to have scattered-light problems that may cause relatively larger errors in the u-band fluxes than other SDSS bands and then perturb the u colors (see the "caveats" on the SDSS websites). In this case, the u colors do not seem to be good estimators of γ^* for our sample.

McGaugh & Schombert (2014) found that the solar metallicity model from Schombert & Rakos (2009) changes in color as it ages from 1 to 12 Gyr by $\Delta(B-V) = 0.37$ and $\Delta(J-K) = 0.03$, demonstrating that NIR colors (such as

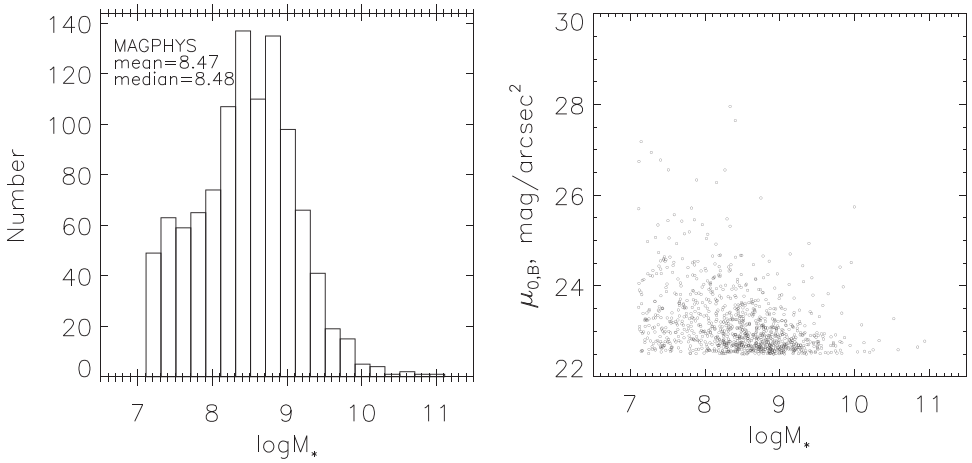

Figure 6. Stellar masses for the R sample derived from the SED fitting using MAGPHYS. The left panel is the distribution histogram of stellar mass, log M_*, vs. central surface brightness, $\mu_{0,B}$, that is measured in Du et al. (2015) and given in Du et al. (2019).

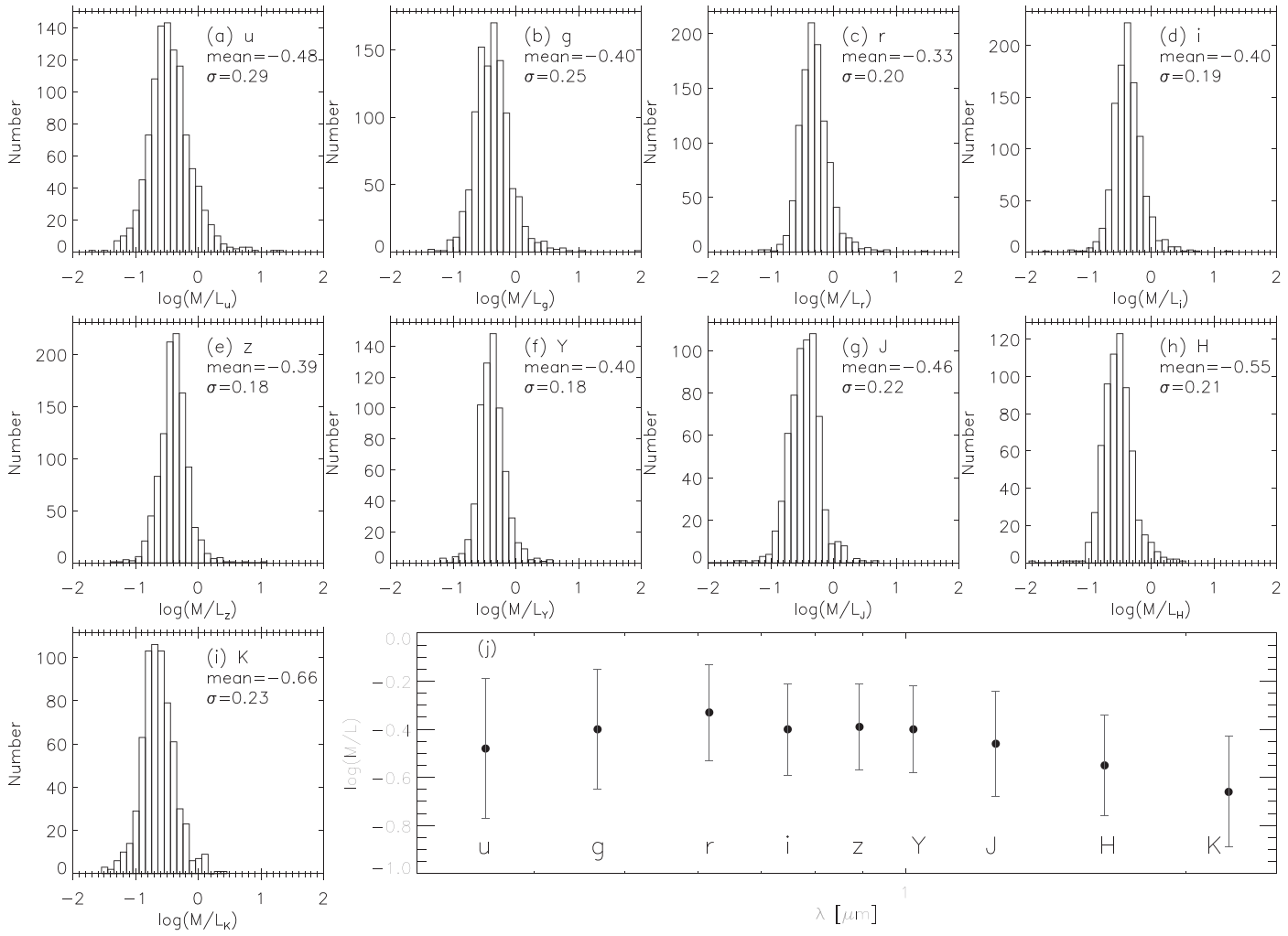

Figure 7. Distribution of stellar *M/L* ratios based on luminosities in each band from the FUV to *K* bands.

$J-H$, $J-K$, and $H-K$ here) are much less sensitive indicators of γ^* than optical colors. Thus, it is expected that using NIR colors as a γ^* estimator results in nearly zero PCCs in Table 2, and the $g-r$ and $g-i$ colors with the greatest PCCs (mostly >0.5) are instead more sensitive indicators of γ^* in the g, r, i, and z bands for our sample. The PCCs are declining as the wavelength band goes redder. This is because the variation of γ^* with color is expected to be minimized in the NIR, so the γ^* in an NIR band is almost a constant, being independent of colors. In this case, we would only focus on investigations of independently using $g-r$ and $g-i$ colors as estimators of γ^* measured in the *griz* bands. We show "robust"

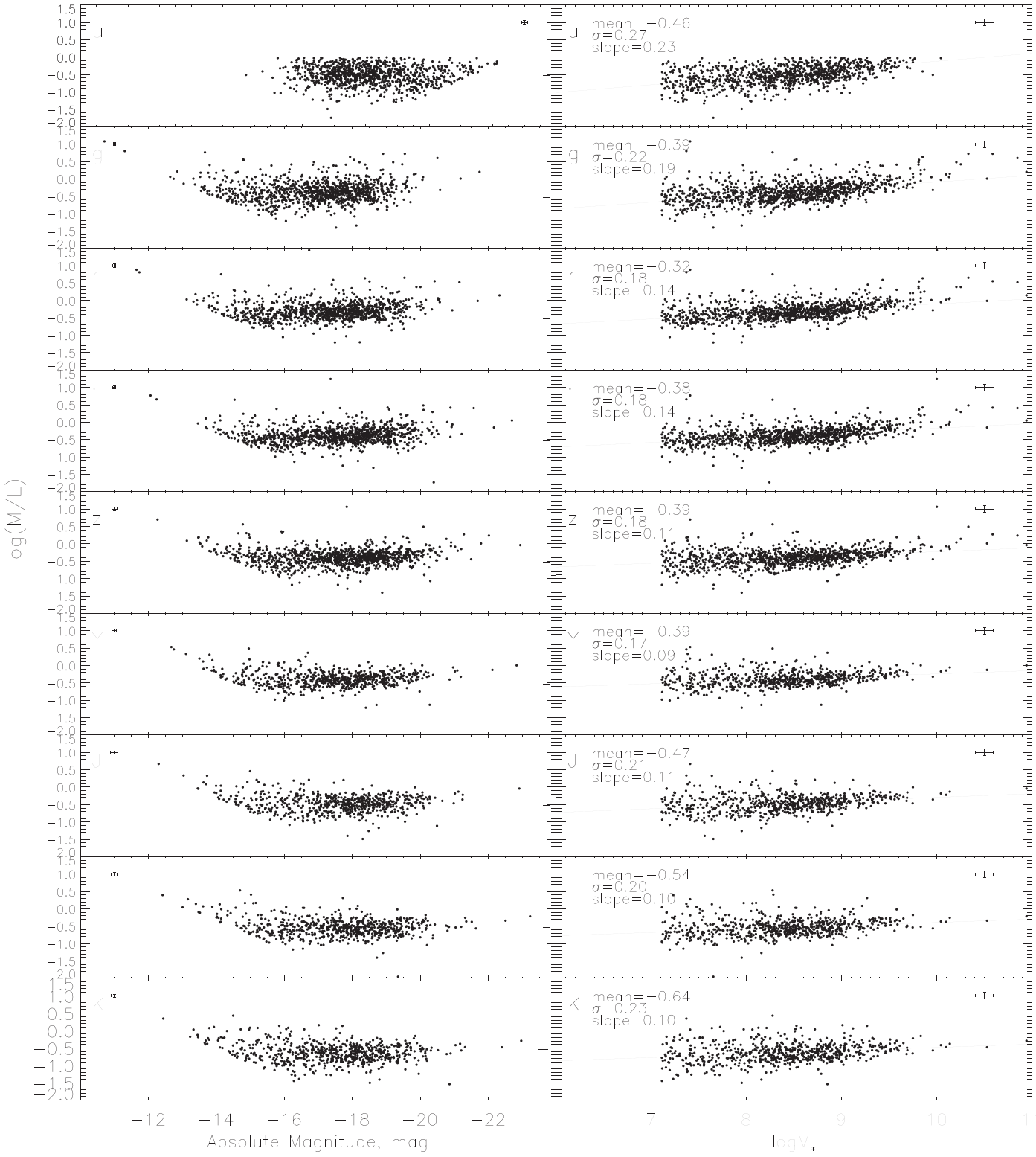

Figure 8. The R LSBG sample in the γ^*–absolute magnitude (left) and γ^*–stellar mass (right) planes. Here stellar masses measured in the *ugrizYJHK* bands are shown from top to bottom, respectively. To prevent the picture from being a vague blob, only the average error bars in both axes are given in each panel. It should be noted that the error of absolute magnitude in the *x*-axis is from a mathematical propagation of the errors of galaxy magnitude (measured by SExtractor) and galaxy distance (directly given in the ALAFLFA catalog; Haynes et al. 2018), and the error of γ^* in the *y*-axis is from a mathematical propagation of the errors of stellar mass, M_* (estimated by the MAGPHYS code), and galaxy luminosity (measured by SExtractor).

bi-square-weighted line fits (black solid lines) of $\log \gamma^j_*$ ($j = g$, r, i, and z) with $g - r$ color in the left column of Figure 9 and $g - i$ color in the left column of Figure 10. The coefficients of the bi-square-weighted line fitting relations are tabulated in Table 3, which provides a direct comparison with tables in other published papers, such as Table 7 of Bell et al. (2003) and Table B1 of Zibetti et al. (2009). The detailed comparison will be presented in Section 5.2.

Table 2
PCCs for the MLCRs

Color	PCC_g	PCC_r	PCC_i	PCC_z	PCC_J	PCC_H	PCC_K
$u-g$	0.02	0.05	0.01	0.24	0.00	0.04	0.06
$u-r$	0.25	0.24	0.20	0.40	0.20	0.21	0.09
$u-i$	0.26	0.28	0.19	0.47	0.21	0.22	0.13
$u-z$	0.48	0.47	0.49	0.21	0.38	0.37	0.30
$g-r$	0.65	0.49	0.56	0.39	0.49	0.45	0.36
$g-i$	0.67	0.61	0.48	0.59	0.51	0.42	0.37
$g-z$	0.49	0.46	0.52	0.02	0.43	0.38	0.39
$r-i$	0.11	0.17	0.03	0.29	0.07	0.06	0.04
$r-z$	0.28	0.31	0.34	0.16	0.22	0.25	0.29
$J-H$	0.09	0.04	0.03	0.02	0.29	0.17	0.08
$J-K$	0.00	0.06	0.06	0.02	0.16	0.03	0.27
$H-K$	0.09	0.10	0.11	0.02	0.07	0.11	0.30

5.2. Comparison with Other Color–γ^* Relations

The γ^*s of galaxies in this work are derived by fitting SPS models to the observed SEDs, so the derived γ^* (hence the stellar MLCR) should be dependent on SPS models, since different SPS models do not usually take the same prescription for the primordial ingredients, including the assumption of IMF, the stellar evolution theory in the form of isochrones, the treatment of SFH, metallicity distribution, and thermally pulsing asymptotic giant branch (TP-AGB) phase. Therefore, we compare our MLCRs with several other representative MLCRs of Bell et al. (2003, hereafter B03), Zibetti et al. (2009, hereafter Z09), Into & Portinari (2013, hereafter IP13), Roediger & Courteau (2015; RC15) based on the Bruzual & Charlot (2003; BC03) (hereafter RC15(BC03)) and and Conroy et al. (2009; FSPS) (hereafter RC15(FSPS)) models, and Herrmann et al. (2016, hereafter H16). Since our relations (and those of Z09, RC15, and H16) are based on a Chabrier (2003) stellar IMF, while B03 is based on a "diet" Salpeter IMF and IP13 is based on a Kroupa (1998) IMF, we have applied zero-point offsets for the MLCRs of B03 and IP13 for a better comparison. It was noted by B03 that $\log\gamma_*$ should be added by 0.15, 0.0, −0.1, −0.15, −0.15, −0.15, and −0.35 dex to be converted from their "diet" Salpeter IMF to the Salpeter (1955), Gould et al. (1997), Scalo (1986), Kroupa et al. (1993), Kroupa (2002), Kennicutte (1983), or Bottema 63% maximal IMFs. We follow Gallazzi et al. (2008) and Zibetti et al. (2009) to reduce the B03-predicted $\log\gamma_*$ by −0.093 dex to convert from the "diet" Salpeter IMF to a Chabrier (2003) IMF. Following H16, we added 0.057 dex to the IP13-predicted $\log\gamma_*$, which is based on a Kroupa IMF to adjust to a Chabrier IMF.

With all of the literature MLCRs adjusted (if needed) to a Chabrier IMF, we overplot the relations of $\log\gamma_*^j$ ($j = g$, r, i, and z) with $g-r$ color in the left column of Figure 9 and $g-i$ color in the left column of Figure 10 with different colored dashed lines. In comparison to each other, the B03 MLCR (red line) has the shallowest slope, and the Z09 MLCR (blue line) has the steepest slope of all the colored lines in each panel, and our linear fitting line (black solid line) for the LSBG data is among these colored literature MLCRs in each panel. The B03 MLCRs (red dashed lines) do not appear to fit our LSBG data well, and they overestimate the γ^*s for our LSBGs in all panels. In quantity, we show the distributions of both B03 MLCR-based (red) and our MLCR-based (black) γ_* for our LSBGs in Figure 11 and roughly derive a systematic offset $\Delta\log\gamma_*^j = 0.26$ dex for $j = g$ and r (predicted from $g-r$ color) between BC03 and our MLCRs. The IP13 (green dashed lines) and RC15(FSPS) (gray dashed lines) MLCRs are slightly higher in all panels, whereas the Z09 (blue dashed lines) and RC15(BC03) (cyan dashed lines) MLCRs fit our LSBG data well and match our fitting lines (except for being a little steeper).

Such differences between the MLCRs from various studies are probably due to the variety of galaxy samples, linear fitting technique, and SED model ingredients mainly consisting of stellar population (SP) model, IMF, and SFH. All of these factors are discussed in Section 6.

6. Discussion of Variance between MLCRs

6.1. Variety of Galaxy Samples

The B03 MLCR is based on a sample of mostly bright (13 mag $\leqslant r \leqslant$ 17.5 mag) HSBGs ($\mu_r < 21$ mag arcsec^{-2}). The vast majority of their galaxies have 0.4 mag $< g-r <$ 1.0 mag in color (as shown in Figure 5 in Bell03). The RC15 MLCR is based on a representative sample of nearby bright galaxies with apparent B-band magnitudes >16 mag from the Virgo cluster.

The IP13 and Z09 MLCRs are purely theoretical. The IP13 MLCR is based on a combination of simple stellar populations (SSPs) from the isochrone data set of the Padova group, which includes a revised (new) prescription for the TP-AGB, composite stellar populations that are generated by convolving SSPs according to exponentially declining (or increasing) SFHs, and disk galaxy models from Portinari et al. (2004). The Z09 MLCR is based on a Monte Carlo library of 50,000 SSPs from CB07, assuming a two-component SFH of a continuous, exponentially declining mode with random bursts superimposed, and also includes a revised (new) prescription for the TP-AGB phase. Although they strive to construct a representative sample of the whole galaxy populations, they are all biased to HSBGs and redder galaxies to varying degrees. For example, the B03 sample lacks sufficient LSBGs and bluer galaxies ($g-r < 0.4$ mag), which would cause a weak constraint for the MLCR in the bluer color part but be more constrained by the redder galaxies with $g-r > 0.4$ mag. However, our MLCR is calibrated for a sample of LSBGs (most of which have $\mu_r > 21$ mag arcsec^{-2} and $r > 17.5$ mag), and 73% of the sample is bluer than $g-r = 0.4$ mag, with the rest in the range 0.4 mag $< g-r <$ 1.0 mag. This work is hitherto the first attempt to test the MLCR on LSBGs that are proposed to be potentially different from HSBGs. In this case, we additionally overplot the H16 MLCR (magenta dashed lines), which is based on a sample of 34 dwarf irregular (dIrr) galaxies in the corresponding panels in the left column of Figure 9, since H16 only gives the MLCR of $\log\gamma_*^j$ ($j = g$ and r) with $g-r$ color. It seems that the H16 MLCR is much flatter than the B03 MLCR. Therefore, the distinction/disparity between sample properties may lead to subtle/significant differences between the MLCRs.

In addition, both our and B03's MLCRs are based on photometry measured on SDSS images, but the methods of photometry are different between us. The SDSS Petrosian (SDSS Petro) magnitudes are adopted by B03 and measured within a circular aperture that is twice the radius at which the local surface brightness is 1/5 of the mean surface brightness within that radius. As we mentioned in Section 2.3, the SDSS Petro has been reported to underestimate the magnitudes of

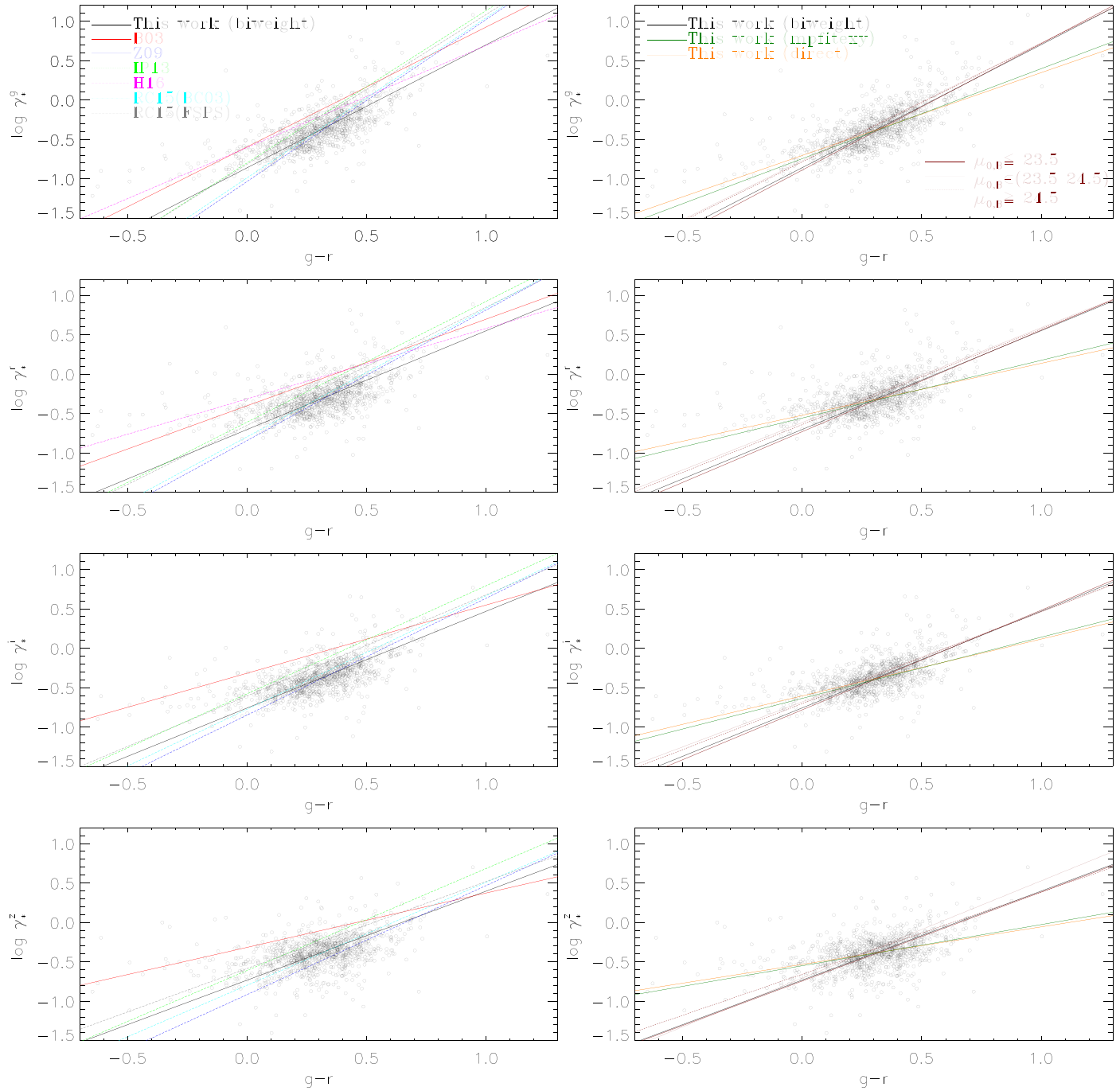

Figure 9. Comparison of estimated *g*-, *r*-, *i*-, and *z*-band stellar γ^* ratios as a function of $g - r$ color for LSBGs in this paper (black circles). In all panels, we show our correlation by a "robust" bi-square-weighted line fit (solid black line) with the assumption of a Chabrier (2003) IMF and the CB07 SP model. For comparison, we overplot the correlations of Bell et al. (2003; B03) as the red line, Zibetti et al. (2009; Z09) as the blue line, Into & Portinari (2013; IP13) as the green line, Herrmann et al. (2016; H16) as the magenta line, Roediger & Courteau (2015) based on the BC03 model (RC15(BC03)) as the cyan line, and Roediger & Courteau (2015) based on the FSPS model (RC15(FSPS)) as the grey line in each panel. All the CMLRs from literatureshown here are under or have been corrected under the Chabrier (2003) IMF. We note that the color–*M*/*L* correlations are in the form of $\log_{10}(M/L) = a_\lambda + b_\lambda \times$ color.

bright galaxies by ∼0.2 mag (He et al. 2013) and dwarf galaxies by up to ∼0.5 mag (Lisker et al. 2007) due to its sky estimate algorithm that tends to subtract the low surface brightness parts of galaxies as part of the sky background. To correct this problem, B03 roughly subtracts 0.1 mag from the SDSS Petro magnitudes for their sample galaxies. However, for our LSBGs, we take a more accurate sky estimate method (Zheng et al. 1999; Wu et al. 2002; Du et al. 2015) in advance to generate an "unbiased" 2D sky background for each of the SDSS images. The sky-subtracted images are then fed into the SExtractor code to measure the magnitudes of our LSBGs within the Kron elliptical aperture (SEx AUTO; recommended by SExtractor), which is distinct from the SDSS Petro circular aperture that B03 adopts. Hill et al. (2011) tested the mean (median) difference between SDSS Petro circular aperture magnitude and the SExtractor Kron elliptical aperture magnitude for the same galaxy sample and found that the offset is 0.04 (−0.01), 0.03 (0.01), 0.02 (0.01), 0.04 (0.01), and 0.02

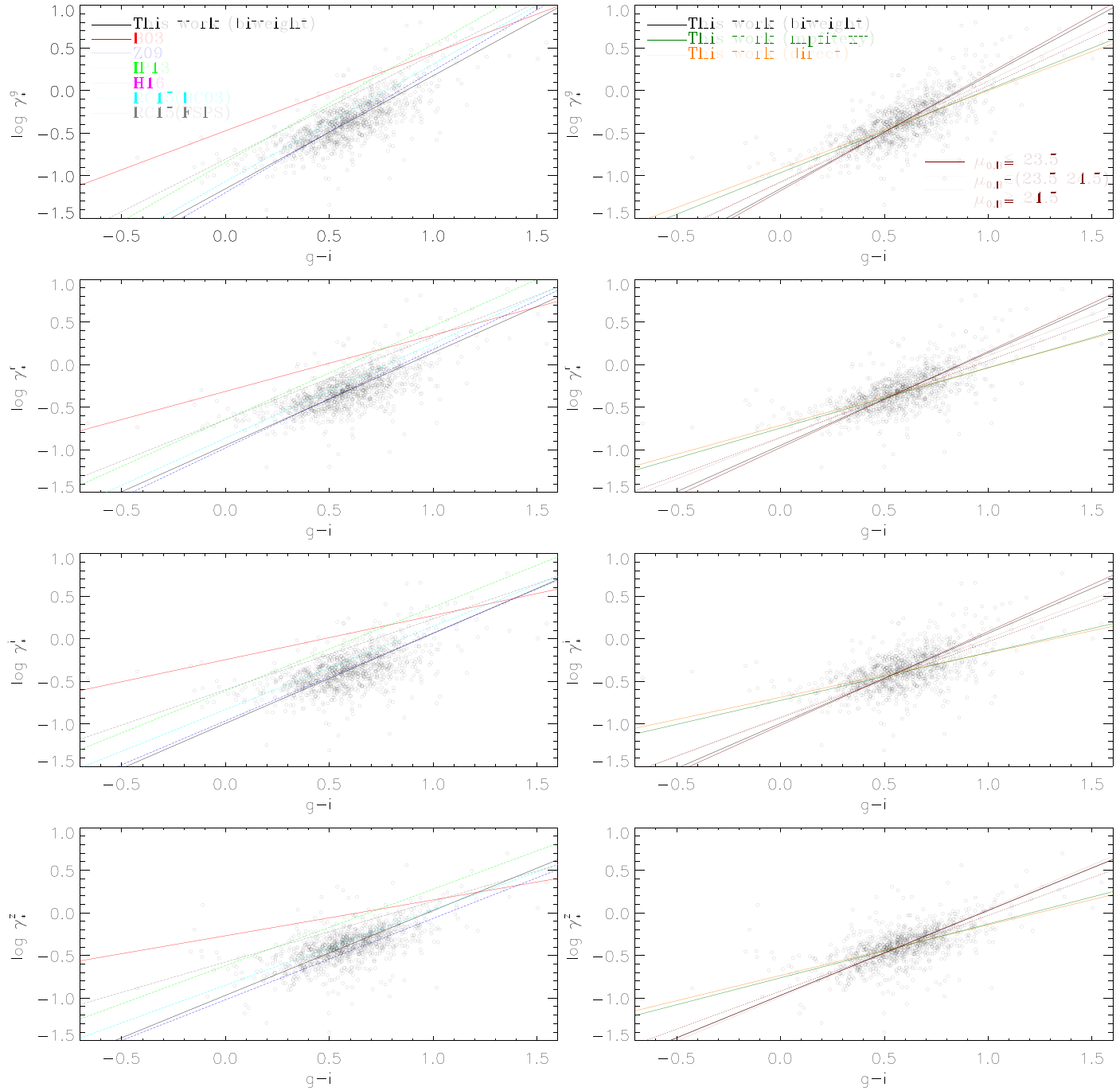

Figure 10. Comparison of estimated *g*-, *r*-, *i*-, and *z*-band stellar γ^* ratios as a function of $g - i$ color for LSBGs in this paper (black circles). In all panels, we show our correlation by a "robust" bi-square-weighted line fit (solid black line) with the assumption of a Chabrier (2003) IMF and the CB07 SP model. For comparison, we overplot the correlations of Bell et al. (2003; B03) as the red line, Zibetti et al. (2009; Z09) as the blue line, Into & Portinari (2013; IP13) as the green line, Herrmann et al. (2016; H16) as the magenta line, Roediger & Courteau (2015) based on the BC03 model (RC15(BC03)) as the cyan line, and Roediger & Courteau (2015) based on the FSPS model (RC15(FSPS)) as the grey line in each panel. All the CMLRs from literatureshown here are under or have been corrected under the Chabrier (2003) IMF. We note that the color–*M*/*L* correlations are in the form of $\log_{10}(M/L) = a_\lambda + b_\lambda \times$ color.

(−0.01) mag in the *u*, *g*, *r*, *i*, and *z* bands, respectively. Obviously, the offset of magnitudes arising from the difference between the two aperture definitions is small. Here we also tested the difference between SEx AUTO and SDSS Petro (from the SDSS DR7 photometric catalog) magnitudes for our sample. As shown in Figure 12, the mean (median) offset of SEx AUTO from SDSS Petro magnitudes is 0.18 (0.26), 0.16 (0.23), 0.09 (0.14), 0.31 (0.37), and 0.52 (0.62) mag, respectively, in the *u*, *g*, *r*, *i*, and *z* bands. Compared to the results of Hill et al. (2011), these offsets for our LSBGs are larger, which is mainly due to our correction for the underestimation of SDSS Petro magnitude by using a different but better sky subtraction recipe (Section 2.3) from the SDSS one. Apparently, these offsets in magnitude for our sample are reasonably consistent with the expected correction value for sky subtraction provided in previous literature (e.g., Lisker et al. 2007; He et al. 2013), but it will also cause the offset of zero-point (color and log γ_*) between B03 and our MLCRs

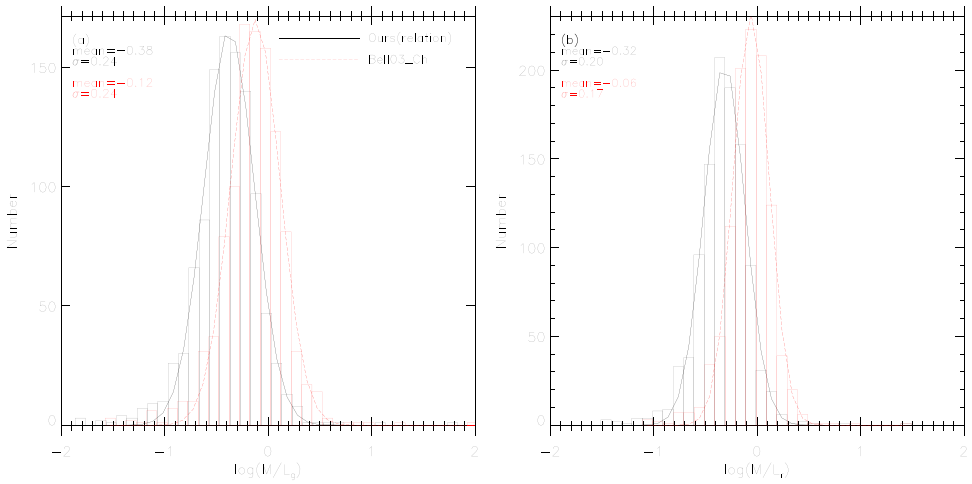

Figure 11. Comparisons of g-based (left) and r-based (right) γ^*s predicted from B03 color–M/L correlations (converted to the Chabrier 2003 IMF; red) with those predicted from our correlations (black) for our LSBG sample. In each panel, each histogram is fitted by a Gaussian profile to derive a mean and σ of the γ^*, showing that the B03 correlations systematically overestimate the γ^* by ∼0.26 dex for our LSBG sample. It should be noted here that legend Bell03_Ch refers to B03, the IMF of which has been corrected to the Chabrier (2003) IMF.

Table 3
The Fitting Parameters for the MLCRs in the Form of $\log(\gamma^*) = a_\lambda + (b_\lambda \times$ color)

Color	a_g	b_g	a_r	b_r	a_i	b_i	a_z	b_z
$g - r$	−0.857	1.558	−0.700	1.252	−0.756	1.226	−0.731	1.128
$g - i$	−1.152	1.328	−0.947	1.088	−0.993	1.057	−0.967	0.996

because the B03 MLCR subtracts 0.1 dex from the SDSS Petro magnitudes of their galaxies to correct the sky subtraction problem of the SDSS photometry. However, for our sample, our mean correction values for SDSS Petro magnitudes in the g, r, i, and z bands are −0.16, −0.09, −0.31, and −0.52 mag, respectively, while according to the B03 method, the correction value would be −0.1 mag for all four bands. So, our correction would result in a mean offset of ∼−0.07 in $g - r$ and 0.15 mag in $g - i$ color zero-points from the B03 correction for our sample, which implies that our sample would systematically shift redward by $\Delta(g - r) \sim 0.07$ mag in all panels of the left column of Figure 9 but blueward by $\Delta(g - r) \sim 0.15$ mag in all panels of the left column of Figure 10, if the B03 correction was applied to our sample. In this similar way, we can derive that our sample would shift upward by $\Delta\log\gamma^j_* \sim 0.02$, 0.0, 0.08, and 0.17 dex for $j = g$, r, i, and z in the corresponding panels in Figures 9 and 10, if the B03 correction was applied to our sample.

So, in most panels, the systematic shifts of our sample blueward in color and especially upward in γ^* would reduce the offset between our sample and the B03 MLCR, although they cannot completely eliminate the disparity between our sample and the B03 MLCR obviously shown in Figures 9 and 10.

6.2. Fitting Techniques

The MLCRs are given by fitting the galaxy data to linear lines. In Section 5, we fit linear MLCRs (black solid lines in the left column of Figures 9 and 10) to our LSBG data by using a bi-square weight technique (biweight), which uses the distance perpendicular to the bisecting line of the data to calculate weights of data points for fitting and was also adopted by the B03 MLCRs. Since diverse fitting techniques may result in distinguishing coefficients for the fitting line, we show the fitting lines by using another two different line fitting techniques for our LSBG data in the right column of Figures 9 and 10. The dark green line in each panel is given by the MPFITEXY, an IDL fitting procedure, which finds the best-fitting straight line through data with errors in both coordinates, taking into consideration the calculation of weights for each data point. The orange line in each panel is given by a direct fitting method, which directly fits the LSBG data to a linear model by minimizing the χ^2 with no weights considered for fitting. For a clear comparison, the black solid line previously given by the biweight fitting technique is also overplotted in each panel of the right column of Figures 9 and 10, and the coefficients of the MLCRs given by the three different line fitting methods for our LSBG data are also tabulated in Table 4. Obviously, in each panel, the MPFITEXY (dark green line) and direct (orange line) techniques give closely consistent fitting lines that are much flatter than the biweight fitting line (black solid line), agreeing much better with the flatter B03 MLCR in slope in each panel in the right column of Figures 9 and 10. This reveals that the results of the fitting line are more or less dependent on the fitting technique, and we cannot guarantee that our fitting technique is completely the same as the techniques used by other literature MLCRs.

6.3. SED Model Ingredients

The basis of using the SED fitting method to estimate stellar mass or γ^* is that galaxies can be viewed as a convolution of SSPs of different ages and metallicities, according to a specific star formation and chemical evolution history (SFH). So far, there are various SP models, e.g., Vazdekis et al. (1996, hereafter Vazdekis model), Fioc & Rocca-Volmerange (1997, hereafter PEGASE model), Bruzual & Charlot (2003, hereafter BC03

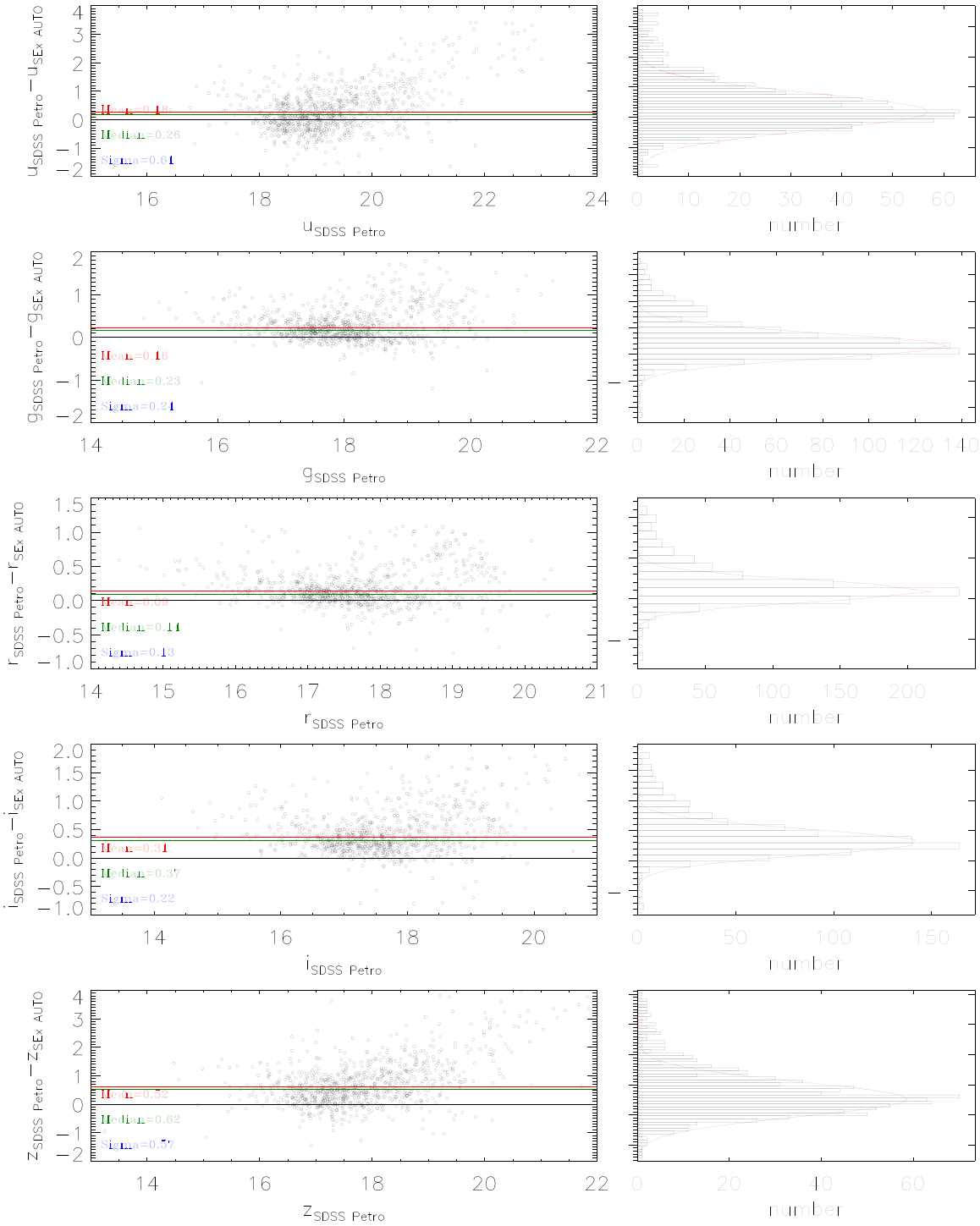

Figure 12. Comparison of SEx Kron elliptical aperture magnitude measured with SExtractor with the SDSS Petro magnitude in the *ugriz* bands for our LSBG sample. The left panel for each band shows the difference (SEx Kron—SDSS Petro) in magnitude versus SDSS Petro. In each of the left panels, the black line is the zero difference line. Excluding the outlier points outside $\pm 3\sigma$, the robust mean (red line) and median (green line) difference in magnitude and the scatter, σ, are listed in each of the left panels for each band. The right panels show the histogram distributions of the difference in each band.

model), the 2007 version of BC03 (hereafter CB07), and Conroy et al. (2009, hereafter FSPS model). These models are based on various stellar evolutionary tracks or isochrones, stellar libraries, and the prescriptions for the late stage of evolution, such as the TP-AGB phase, assuming various IMFs and SFHs.

For the MLCRs in the figures, RC15 uses two independent SP models of BC03 (RC15(BC03)) and FSPS (RC15(FSPS)), as shown in the MLCR figures. The FSPS model (gray dashed line) always gives a flatter MLCR than the BC03 model (cyan dashed line) in each panel. This demonstrates that the choice of SP model matters a lot, which would result in distinguishing MLCRs, especially in slope. The PEGASE model is adopted by B03, incorporating an "old" prescription (Girardi et al. 2000, 2002) for TP-AGB stars. The new Padova model (SSP

Table 4
The Coefficients for the MLCRs from Three Different Line Fitting Methods for Our LSBG Data in the Form of $\log(\gamma^*) = a_\lambda + (b_\lambda \times \text{color})$

Color	a_g	b_g	a_r	b_r	a_i	b_i	a_z	b_z
Biweight (Black Solid Line)								
$g-r$	−0.857	1.558	−0.700	1.252	−0.756	1.226	−0.731	1.128
$g-i$	−1.152	1.328	−0.947	1.088	−0.993	1.057	−0.967	0.996
Direct (Orange Solid Line)								
$g-r$	−0.709	1.072	−0.526	0.672	−0.607	0.732	−0.537	0.490
$g-i$	−0.924	0.932	−0.719	0.691	−0.691	0.530	−0.741	0.606
MPFITEXY (Dark Green Solid Line)								
$g-r$	−0.743	1.141	−0.556	0.732	−0.635	0.775	−0.550	0.522
$g-i$	−0.964	0.976	−0.744	0.708	−0.723	0.563	−0.762	0.633

model generated from the isochrones of Padova group) was used by IP13, and Z09, H16, and our MLCRs are all based on the CB07 model, which incorporates a "new" prescription (Marigo & Girardi 2007; Marigo et al. 2008) for TP-AGB stars. The "new" treatment for the TP-AGB phase includes a larger contribution from TP-AGB stars that change little from the optical luminosity dominated by main-sequence stars, greatly enhances the predicted redder/NIR luminosity of galaxies, and finally leads to lower γ^* in redder/NIR bands than bluer bands. This is why the disparity between B03 (red dashed line) and our MLCRs (black solid line) in the MLCR figures is becoming larger in panels of red bands of the i and z bands than those of the g and r bands for our sample.

The IMF is critical for determining the γ^* of a galaxy from the SED fitting method. The extant IMFs are mostly determined for the Milky Way in the solar neighborhood, while the IMF of external galaxies is, in principle, unknown (Courteau et al. 2014). The various IMFs, e.g., the Salpeter (Salpeter 1955), Kroupa (Kroupa 1998, 2001), and Chabrier (Chabrier 2003) IMFs, differ mainly in the slope for low-mass stars, which serve mostly to change the mass without much changing the luminosity or color. So an IMF that includes more low-mass stars, such as the Salpeter IMF, yields a higher γ^* at a given color, since the large number of low-mass stars would greatly increase the stellar mass but hardly affect the luminosities or colors of galaxies, as these stars are too faint. Hence, different IMFs would result in offsets in the zero-point of the MLCRs, even though the relation slopes may remain unchanged (Bell & de Jong 2001; Bell et al. 2003; Courteau et al. 2014). In our modeling, we assumed a Chabrier IMF, which gives small number of low-mass stars. However, the B03 MLCR assumed a "diet" Salpeter (1955) IMF, which gives a larger number of stars in the low-mass end of IMF and thus yields a higher γ^* at a given color than the Chabrier IMF. The IP13 MLCR uses a Kroupa (1998) IMF. However, we have converted both the B03 and IP13 MLCRs from their original IMFs to a Chabrier IMF by adding a correction value to the originally predicted log $\gamma_* f$ for comparison in the left column of the MLCR figures (Figures 9 and 10). If we choose the correction value to be −0.093 dex for the B03 MLCR following Gallazzi et al. (2008) and Zibetti et al. (2009) and 0.057 dex for IP13 following Herrmann et al. (2016), the IMF-corrected B03 MLCR (red dashed line) shown in the MLCR figures is still higher than our MLCR; however, the IMF-corrected IP13 (green dashed line) appears more consistent with our MLCR in the zero-point in each panel of the MLCR figures. If the correction values changed, the zero-points of both MLCRs would shift accordingly. So the zero-points of the IMF-converted B03 and IP13 MLCRs in the figures should still be dependent on the uncertainties of the correction values that we do not know for sure. Besides, we are not certain about whether the correction values used here are accurate, as −0.093 dex is used in H16, while −0.15 is used in RC15. Similar to our MLCR, the Z09 (blue dashed line) and RC15(BC03) (cyan dashed line) MLCRs also use a Chabrier IMF, so they are obviously going to be more consistent with our MLCR in zero-point than other literature MLCRs in the figures. Unlike RC15(BC03), the RC15(FSPS) MLCR (gray dashed line) has an relatively larger offset from our MLCR because it uses a different SP model of FSPS, although it also uses a Chabrier IMF. This will be discussed later. Although the H16 (magenta dashed lines in the first two panels) MLCR uses a Chabrier IMF, it is much higher (like B03) than our MLCR in each panel. This should be due to the different line fitting technique (as discussed in Section 6.2) and other different SPS model ingredients that will be discussed later.

The SFH regulates the star formation and chemical enrichment with time. The choice of the SFH, in particular whether it is rising, declining, or bursty, can significantly change the best-fit stellar mass by perhaps as much as 0.6 dex in extreme cases (Pforr et al. 2012; Conroy 2013). An exponentially declining (or increasing) SFH in the form of $\Psi(t) = e^{-t/\tau}$ is considered by IP13. The declining ones are modeled with e-folding timescales τ ranging from 1.55 Gyr to ∞ (constant SFR), and the increasing ones are modeled with negative values of τ ranging from −50.00 to −1.00. The H16 MLCR is based on a library of multicomponent complex SFHs that was created for dIrr galaxies by Zhang et al. (2012) and totally different from the commonly used two-component SFH model from the literature. Our MLCRs, RC15's MLCRs, and Z09's MLCRs are all based on the two-component SFH model (an exponentially declining SFH with random bursts superimposed), which incorporates a variety of bursty events and allows young ages (of a few Gyr), whereas B03 considers relatively smooth SFHs starting from 12 Gyr in the past and limits the strength of starbursty events (which are simultaneously constrained to only happen in the last 2 Gyr) to $\leqslant$10% by stellar mass. Since a recent burst of star formation will dramatically lower the mass-to-light ratio of a total stellar system than a smooth star formation model by up to 0.5 dex (Courteau et al. 2014), omitting or less burst components from SFH models will bias B03 MLCRs-based γ^* to higher values (Roediger & Courteau 2015).

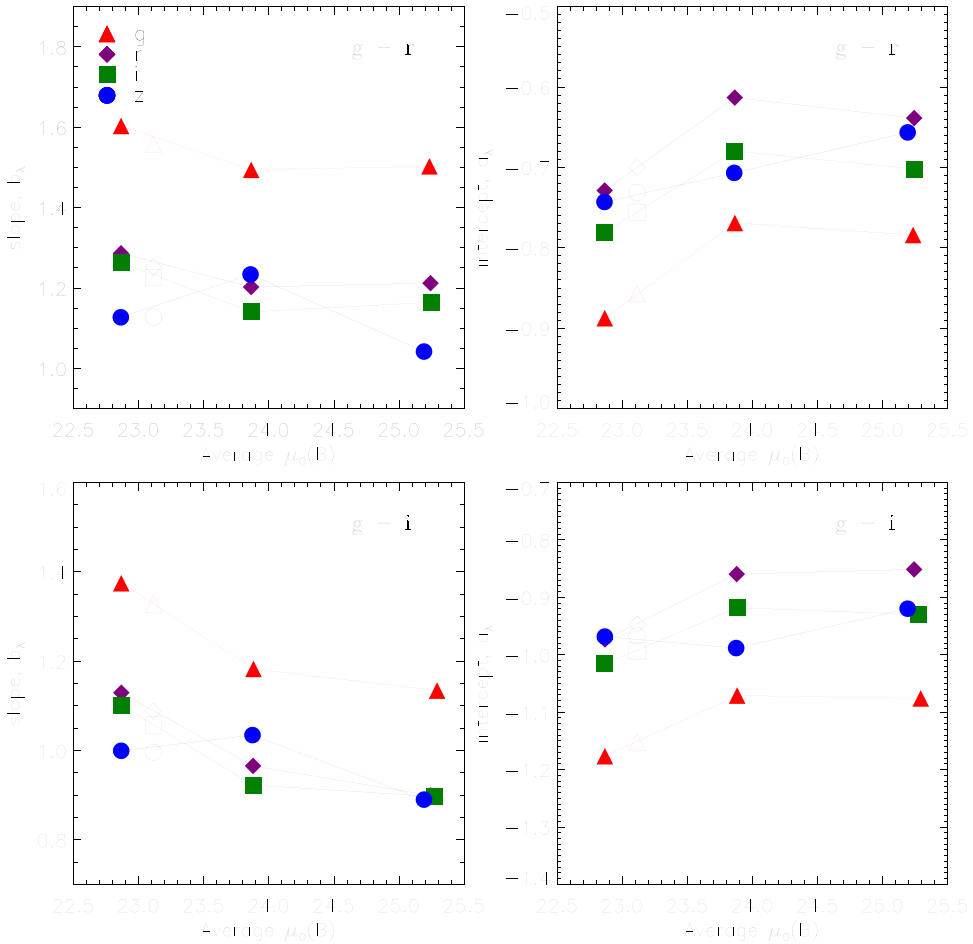

Figure 13. The MLCR linear fit coefficients determined for three different central surface brightness bins where $\log_{10}(M/L) = a_\lambda + b_\lambda \times$ color.

6.4. Effect of Surface Brightness on Fitting Relations

Since a lower surface brightness is the characteristic that distinguishes LSBGs from HSBGs (mostly normal spiral galaxies), here we check whether the MLCRs have a dependence on galaxy surface brightness, besides the external factors discussed above. We divide our LSBG data into three central surface brightness bins ($\mu_{0,B} \leqslant 23.5$, $23.5 < \mu_{0,B} < 24.5$, and $\mu_{0,B} \geqslant 24.5$). These B-band central surface brightness are all measured in Du et al. (2015). Then, we fit the MLCR for galaxies in each bin using the biweight line fitting technique. The MLCR for each bin is overplotted (as three brown lines of different styles) in each panel in the right column of Figures 9 and 10. It is obvious that the MLCRs slightly flatten with the lower central surface brightness, as shown in Figure 13. However, the change of MLCR due to the change of central surface brightness (represented by the differences between the black and brown lines) is small, which is far less than that due to the change of fitting techniques (shown by the larger offset between the black and dark green/orange lines) in the right column of the MLCR figures.

In this case, we think the minor differences between our MLCRs (for LSBGs) and the literature MLCRs (for the whole galaxy population, HSBGs, or dwarfs) are more caused by the combination of differences in SED fitting models (IMF, SFH, and SPS), the photometric zero-point of the data, and line fitting techniques, rather than the central surface brightness of the galaxies themselves. As shown in the left column of the MLCR figures, our MLCR (black solid line) for LSBGs is among the literature MLCRs in each panel, so it is expected to be generally consistent with those literature MLCRs for various samples, if those main factors of difference in photometric methods, line fitting methods, and models (IMF, SFH, and SPS) are taken into account. This could be further in evidence by the best consistency between our MLCR and the Z09 MLCR (blue dashed line), especially in Figure 10, which is based on the same IMF, SPS model (CB07), and SFH as our MLCR but based on a theoretical library of galaxy samples.

7. Comparison with Huang12's Stellar Mass for Dwarf Galaxies

In this section, we hope to assess our MLCRs by comparing the predicted stellar masses with those estimated in an independent paper (Huang et al. 2012, hereafter Huang12) for dwarf galaxies with comparable properties.

Huang12 defined a sample of gas-rich dwarf galaxies that have $\log M_{\rm H\,I} < 7.7$ and $W50 < 80\,{\rm km\,s^{-1}}$ from the $\alpha.40$ H I survey catalog. They gave stellar masses for these sample galaxies by fitting their SEDs consisting of *GALEX* (FUV and NUV) and SDSS (*ugriz*) photometric bands to the BC03 model, assuming a Chabrier (2003) IMF and a continuous SFH with random bursts superimposed, which are the same as our assumptions. Besides the SED fitting results, Huang12 also predicted the stellar masses according to the B03 MLCR (i versus $g - r$). In comparison, their SED fitting yields a

median log $M_*/M_\odot = 7.45$, while the B03 MLCR (converted to a Chabrier IMF) gives a considerably higher median of 7.73, which overestimates the stellar mass by ∼0.28 dex. Using Huang12's criteria, we derive a sample of dwarf galaxies out of our LSBGs. Our MLCR (i versus $g - r$) yields a median log $M_*/M_\odot = 7.36$, while the B03 MLCR (converted to a Chabrier IMF) gives a considerably higher median of 7.69 for our dwarf galaxies, which overestimates the stellar mass by ∼0.33. This result is very similar to Huang12's result in terms of both the stellar mass value and the offset value from B03 predictions, which gives confidence for using our MLCR, especially for dwarf galaxies. The offset should be mainly caused by the ingredients discussed in Section 6, and Huang12 claimed that it is mainly due to the different SFH adopted by Bell03, which does not fully account for the impact of bursty behavior in dwarf galaxies.

8. Summary and Conclusion

We obtained stellar masses, M_*, and γ_* for a sample of LSBGs by fitting their SEDs covering 11 UV, optical, and NIR photometric bands to the SPS model using the MAGPHYS code (da Cunha et al. 2008). The derived M_* for this sample spans from log $M_*/M_\odot = 7.1$ to 11.1 dex, with a mean log $M_*/M_\odot = 8.47$ and a median of 8.48 dex, showing that these LSBGs have a systematically lower M_* than normal galaxies. The γ^* for this sample slightly decreases from the r band to redder wavelength bands for our LSBG sample, similar to the declining trend of γ^* from short to longer wavelengths for normal star-forming galaxies, and the γ^*s vary little with absolute magnitude but slightly increase with higher M_* for our LSBG sample. This increasing trend is stronger in bluer bands, with the steepest slope in u but a nearly flat slope in the K band.

We then fitted the MLCR for the LSBG sample. The log γ^j_* ($j = g, r, i$, and z) have the relatively tightest relations with the optical colors of $g - r$ and $g - i$ for our LSBG data. Compared with the literature MLCRs, our MLCRs are consistently among those literature MLCRs that are converted to the same IMF. The minor differences could be due to the differences in SED models (IMF, SFH, and SPS), photometric zero-points, and line fitting techniques but depend little on the galaxy surface brightness. This may give a possible implication that most of our LSBGs might share generally similar properties in star formation and evolution with the normal galaxies.

We appreciate the anonymous referee for the constructive comments that strengthened this paper. D.W. is supported by National Natural Science Foundation of China (NSFC) grant Nos. U1931109, 11733006, and the Young Researcher Grant funded by the National Astronomical Observatories, Chinese Academy of Sciences (NAOC). C.C. is supported by NSFC grant Nos. 11803044, 11933003, and the Young Researcher Grant funded by NAOC, and in part by the Chinese Academy of Sciences (CAS) through a grant to the CAS South America Center for Astronomy (CASSACA) in Santiago, Chile. Z.Z. is supported by NSFC grant No. 11988101, 11703036, and U1931110. Z.Z. is also supported by CAS Interdisciplinary Innovation Team (JCTD-2019-05) and CAS Key Laboratory of FAST, NAOC, Chinese Academy of Sciences. W.H. is supported by National Key R&D Program of China grant No. 2017YFA0402704 and NSFC grant No. 11733006.

Facilities: *GALEX*, Sloan, UKIRT.

Software: SExtractor (Bertin & Arnouts 1996), MAGPHYS (da Cunha et al. 2008).

ORCID iDs

Wei Du https://orcid.org/0000-0003-4546-8216
Cheng Cheng https://orcid.org/0000-0003-0202-0534

References

Abazajian, K. N., Adelman-McCarthy, J. K., Agüeros, M. A., et al. 2009, ApJS, 182, 543
Bell, E. F., & de Jong, R. S. 2001, ApJ, 550, 212
Bell, E. F., McIntosh, D. H., Katz, N., & Weinberg, M. D. 2003, ApJS, 149, 289
Bertin, E., & Arnouts, S. 1996, A&AS, 117, 393
Bothun, G. D., Impey, C., & McGaugh, S. 1997, PASP, 109, 745
Bruzual, G., & Charlot, S. 2003, MNRAS, 344, 1000, (BC03)
Burkholder, V., Impey, C., & Sprayberry, D. 2001, AJ, 122, 2318
Ceccarelli, L., Herrera-Camus, R., Lambas, D. G., Galaz, G., & Padilla, N. D. 2012, MNRAS, 426, 6
Chabrier, G. 2003, PASP, 115, 763
Charlot, S., & Fall, S. M. 2000, ApJ, 539, 718
Conroy, C. 2013, ARA&A, 51, 393
Conroy, C., Gunn, J. E., & White, M. 2009, ApJ, 699, 486, (FSPS)
Courteau, S., Cappellari, M., de Jong, R., et al. 2014, RvMP, 86, 47
da Cunha, E., Charlot, S., & Elbaz, D. 2008, MNRAS, 388, 1595
Das, M., Reynolds, C. S., Vogel, S. N., McGaugh, S. S., & Kantharia, N. G. 2009, ApJ, 693, 1300
de Blok, W. J. G., McGaugh, S. S., & van der Hulst, J. M. 1996, MNRAS, 283, 18
Du, W., Cheng, C., Wu, H., Zhu, M., & Wang, Y. G. 2019, MNRAS, 483, 1754
Du, W., Wu, H., Lam, M. I., et al. 2015, AJ, 149, 199
Fioc, M., & Rocca-Volmerange, B. 1997, A&A, 326, 950, (PEGASE)
Galaz, G., Herrera-Camus, R., Garcia-Lambas, D., & Padilla, N. 2011, ApJ, 728, 74
Gallazzi, A., Brinchmann, J., Charlot, S., & White, S. D. 2008, MNRAS, 383, 1439
Girardi, L., Bertelli, G., Bressan, A., et al. 2002, A&A, 391, 195
Girardi, L., Bressan, A., Bertelli, G., & Chiosi, C. 2000, A&AS, 141, 371
Gould, A., Behcall, J. N., & Flynn, C. 1997, ApJ, 482, 913
Haberzettl, L., Bomans, D. J., & Dettmar, R.-J. 2007, A&A, 471, 787
Haynes, M. P., Giovanelli, R., Kent, B. R., et al. 2018, ApJ, 861, 49
Haynes, M. P., Giovanelli, R., Martin, A. M., et al. 2011, AJ, 142, 170
He, Y. Q., Xia, X. Y., Hao, C. N., et al. 2013, ApJ, 773, 37
Herrmann, K. A., Hunter, D. A., Zhang, H. X., & Elmegreen, B. G. 2016, AJ, 152, 177
Hill, D. T., Kelvin, L. S., Driver, S. P., et al. 2011, MNRAS, 412, 765
Huang, S., Haynes, M., Giovanelli, R., & Brinchmann, J. 2012, AJ, 143, 133
Hyde, B. J., & Bernardi, M. 2009, MNRAS, 394, 1978
Impey, C., & Bothun, G. 1997, AR&AA, 35, 267
Impey, C., Burkholder, V., & Sprayberry, D. 2001, AJ, 122, 2341
Infante, L. 1987, A&A, 183, 177
Into, T., & Portinari, L. 2013, MNRAS, 430, 2715
Kauffmann, G., Heckman, T. M., White, S., et al. 2003, MNRAS, 341, 33
Kennicutte, R. C. 1983, MNRAS, 272, 54
Kron, R. G. 1980, ApJ, 43, 305
Kroupa, P. 1998, in ASP Conf. Ser. 134, Brown Dwarfs and Extrasolar Planets, ed. R. Rebolo, E. L. Martin, & M. R. Zapatero Osorio (San Francisco, CA: ASP), 483
Kroupa, P. 2001, MNRAS, 322, 231
Kroupa, P. 2002, Sci, 295, 82
Kroupa, P., Tout, C. A., & Gilmore, G. 1993, MNRAS, 262, 545
Lauer, T. R., Faber, S. M., Richstone, D., et al. 2007, ApJ, 662, 808
Lawrence, A., Warren, S. J., Almaini, O., Edge, A. C., Hambly, N. C., et al. 2007, MNRAS, 379, 1599
Lei, F. J., Wu, H., Du, W., et al. 2018, ApJS, 235, 18
Lisker, T., Grebel, E. K., Binggeli, B., & Katharina, G. 2007, ApJ, 660, 1186
Liu, F. S., Xia, X. Y., Mao, S., Wu, H., & Deng, Z. G. 2008, MNRAS, 385, 23
Marigo, P., & Girardi, L. 2007, A&A, 469, 239
Marigo, P., Girardi, L., Bressan, A., et al. 2008, A&A, 482, 883
Martin, D. C., Fanson, J., Schiminovich, D., et al. 2005, ApJL, 619, L1
Matthews, L. D., van Driel, W., & Monnier-Ragaigne, D. 2001, A&A, 365, 1
McGaugh, S. S. 1996, MNRAS, 280, 337

McGaugh, S. S., & Bothun, G. D. 1994, AJ, 107, 530
McGaugh, S. S., Bothun, G. D., & Schombert, J. M. 1995, AJ, 110, 573
McGaugh, S. S., & Schombert, M. J. 2014, AJ, 148, 77
McGaugh, S. S., Schombert, M. J., & Lelli, F. 2017, ApJ, 851, 22
Minchin, R. F., et al. 2004, MNRAS, 355, 1303
O'Neil, K., Bothun, G. D., & Schombert, J. 2000, AJ, 119, 136
O'Neil, K., Bothun, G. D., van Driel, W., & Monnier Ragaigne, D. 2004, A&A, 428, 823
Peng, C. Y., Ho, L. C., Impey, C. D., & Rix, H. 2002, AJ, 124, 266
Pforr, J., Maraston, C., & Tonini, C. 2012, MNRAS, 422, 3285
Portinari, L., Sommer-Larsen, J., & Tantalo, R. 2004, MNRAS, 347, 691
Roediger, J. C., & Courteau, S. 2015, MNRAS, 452, 3209
Salpeter, E. E. 1955, ApJ, 121, 161
Scalo, J. M. 1986, FCPh, 11, 1
Schlafly, E. F., & Finkbeiner, D. P. 2011, ApJ, 737, 103
Schombert, J., & Rakos, K. 2009, AJ, 137, 528
Smith, J., Tucker, D., Kent, S., et al. 2002, AJ, 123, 2121
Trachternach, C., Bomans, D. J., Haberzettl, L., & Dettmar, R. J. 2006, A&A, 458, 341
Vazdekis, A, Casuso, E, Peletier, R. F., & Beckman, J. E. 1996, ApJS, 106, 307
Wilkins, S., Violeta, G., Carlton, B., Lacey, C., & Zuntz, J. 2013, MNRAS, 431, 430
Wu, H., Burstein, D., Deng, Z. G., et al. 2002, AJ, 123, 1364
York, D. G., Adelman, J., Anderson, J. E., Jr, et al. 2000, AJ, 120, 1579
Zhang, H. X., Hunter, D. A., Elmegreen, B. G., Gao, Y., & Schruba, A. 2012, AJ, 143, 47
Zheng, Z., Thilker, D. A., Heckman, T. M., et al. 2015, ApJ, 800, 120
Zheng, Z. Y., Shang, Z. H., Su, H. J., et al. 1999, AJ, 117, 2757
Zibetti, S., Charlot, S., & Rix, H.-W. 2009, MNRAS, 400, 1181